



Numerical simulation of particle flow and segregation during roller spreading process in additive manufacturing

Wenguang Nan ^{a,b}, Mehrdad Pasha ^b, Mojtaba Ghadiri ^{b,*}

^a School of Mechanical and Power Engineering, Nanjing Tech University, Nanjing 211816, China

^b School of Chemical and Process Engineering, University of Leeds, Leeds LS2 9JT, UK

ARTICLE INFO

Article history:

Received 21 August 2019

Received in revised form 26 November 2019

Accepted 12 December 2019

Available online 14 December 2019

Keywords:

Additive manufacturing

Powder spreading

Discrete element method

Particle convection

Segregation

Jamming

ABSTRACT

Additive Manufacturing (AM) using powder spreading requires uniform spreading. For narrow spreader gaps, as commonly used, transient jamming and segregation could adversely affect the uniformity of the spread layer. Here, we consider the dynamics of powder spreading by roller for a gas-atomised metal powder and analyse the effects of gap height and the rotational speed of roller on the evolving particle trajectory and spread layer uniformity by Discrete Element Method. It is shown that transient jamming in narrow gaps and size segregation in the spreading heap, the latter brought about by particle convection/circulation, adversely affect the uniformity of the spread layer. The segregation extent decreases with the increase of gap height or decrease of roller rotational speed. The conditions for uniform spreading are deduced from the simulations.

© 2019 The Authors. Published by Elsevier B.V. This is an open access article under the CC BY license (<http://creativecommons.org/licenses/by/4.0/>).

1. Introduction

Additive Manufacturing (AM) creates three-dimensional (3D) objects by stepwise layer-by-layer building approaches which are controlled by a digital model [1–3]. As a novel production technology for the design and manufacturing of high-performance components, the use of AM is increasing at a fast rate in wide ranging industries, such as aerospace for fuel nozzle, medical technology for prosthetic implants, and heat exchanger in energy applications [4–8]. For example, complex fuel injector nozzles in aerospace technology can now be directly fabricated by AM with lightweight engineered structures, resulting in significant cost savings [9,10]. Amongst several manufacturing methods, the use of powders is attractive in AM as it provides flexibility for a wide range of materials to be used [11,12]. Fine and dry powders in the micrometre size range are typically spread in thin layers by a blade or roller in AM. The spread layer is locally heated by a radiative energy beam to melt or sinter the layer. For this purpose, the spread layer should be very thin, therefore requiring a narrow gap between the spreader and layering base, typically a few multiples of particle diameter. This could cause non-uniformity in the spread layer, making flaws and defects in the structure. Lack of sufficient understanding of this kind of near-boundary flow, such as the shear band within the heap and the transient jamming events occurring in the gap, hinders further advancement in this technology and introduction of new materials for

high quality structures. Poor powder flow during spreading causes variations in the solid volume fraction and deviation of the particle size distribution (PSD) of spread layer from that of the initial feed powder bed, leading to the formation of cavities and heterogeneity, producing inferior products with poor mechanical performance [13–15].

Recently, the Discrete Element Method (DEM) has been used to describe the mechanical behaviour of the powder spreading system in AM [16–31]. Parteli and Pöschel [16] and Haeri et al. [17] studied the effect of spreading conditions on the bed quality in the roller spreading system, and showed that high spreader translational velocity could lead to low bed quality. Chen et al. [18,30] used spherical particles with tuned mechanical properties for DEM simulation in the blade spreading process, and found that the rolling and sliding friction coefficients between particles and the percolation effect in powders with a bimodal particle size distribution had significant effects on the quality of layered powder bed. Haeri [19] identified the optimum blade tip shape to produce a spread layer with volumefraction and surface roughness comparable to a roller under the actual operation conditions. Nan et al. [20] characterised all relevant physical properties and interaction parameters of 316 L steel particles used in DEM simulations, and showed for the first time that transient jamming occurred in narrow spreader gaps and was responsible for the formation of empty patches over the work surface in the blade spreading process. Nan et al. [21] identified a critical blade spreading speed above which the mass flow rate of the powder through the gap was independent of the blade spreading speed, and also showed that the particle velocity in the powder heap in front of the blade could well be described by a universal curve

* Corresponding author.

E-mail address: M.Ghadiri@leeds.ac.uk (M. Ghadiri).

given by the Gauss error function. Meier et al. [22,23] proposed the use of the angle of repose to estimate the surface energy following a calibration procedure. This approach was also adopted by Han et al. [24], who used it in their DEM simulations to identify the optimum layer thickness. However, the surface energy of particles estimated in this approach has not been given, and in any case it would have been affected by various factors in the calibration procedure, such as particle shape, particle size distribution and also particle friction. Herbold et al. [25], Mindt et al. [26], Zhang et al. [27], Lee et al. [28], Fouda and Bayly [29], and Desai and Higgs [31] also identified the factors affecting the layer quality, such as the spreader velocity and layer thickness, where the particles in DEM simulations were considered to be of spherical shape without cohesion. This approach is not representative of real powders used in AM. Moreover, the use of mono size particles in the work of Zhang et al. [27] and Fouda and Bayly [29] brings about a crystalline order to the structure on shearing, which is unrealistic, as slip occurs more readily on planes similar to cleavage planes of crystals. The factors which have not been analysed in detail so far are the segregation of spread layer and the trajectories of particles, which are responsible for the quality of the spread layer. They are directly related to the issues in powder spreading, such as the criterion for the choice of spreading conditions, such as the roller rotational and translational speeds.

In this work, the particle flow in the roller spreading process is simulated by Discrete Element Method. A heap of gas-atomised stainless 316 L steel particles is simulated and subjected to the translational and anti-clockwise rotation of a roller. The particles are spread onto a rough base through a narrow gap between the roller and base. The effects of gap height and roller rotational speed on the particle flow and quality of spread layer are analysed. This provides a step forward in our understanding of the particle convection/circulation in the heap and the consequent size segregation in the spread layer, which is a key factor affecting the production quality.

2. Methods

Gas-atomised 316 L stainless steel particles, provided by Sandvik Osprey Ltd., Neath, UK, are used in this work. Their physical and mechanical properties used in the simulation have previously been characterised by Nan et al. [20], including the interfacial surface energy, Young's Modulus, hardness, restitution coefficient and sliding friction coefficient, as summarised in Table 1 [20]. The particles have a size distribution in the range 15–55 μm , in which the number-based equivalent-circle diameters D_{10} , D_{50} and D_{90} are 20 μm , 32 μm and 45 μm , respectively. They are classified into four main size classes based on their equivalent-circle diameter of the projected area, as shown in Fig. 1(a). The particles shapes for each size class, as viewed by Scanning Electron Microscopy, are shown in Fig. 1(b).

2.1. Discrete element method

To describe the dynamics of particle flow in the spreading process, the particles are modelled as discrete entities and their translational

Table 1
Physical and mechanical properties of particles.

Parameters	Value
Particle diameter, D (mm)	0.045
Particle density, ρ (kg/m^3)	7980
Young's modulus*, E (GPa)	211
Poisson ratio, ν	0.3
Friction coefficient, μ	0.5
Restitution coefficient, e	0.64
Surface energy*, γ (mJ/m^2)	9.0

*Young's modulus is scaled down to 2.1 GPa, and surface energy is correspondingly scaled down to 1.4 mJ/m^2 in the DEM simulation, based on approach of Behjani et al. [36] and Hærvig et al. [37].

and rotational motions are tracked individually by solving Newton's laws of motion [32–34], for which the EDEM™ software package provided by DEM Solutions, Edinburgh, UK, is used:

$$m_i \frac{d\mathbf{v}_i}{dt} = \sum \mathbf{F}_{c,i} + m_i \mathbf{g} \quad (1)$$

$$\frac{d(\mathbf{I}_i \cdot \boldsymbol{\omega}_i)}{dt} = \mathbf{R}_i \cdot \sum \mathbf{M}_{c,i} \quad (2)$$

where m_i , \mathbf{I}_i , \mathbf{v}_i and $\boldsymbol{\omega}_i$ are the mass, moment of inertia, translational velocity and angular velocity, respectively; $\mathbf{F}_{c,i}$ is the contact force, originating from its interaction with neighbouring particles or walls; $\mathbf{M}_{c,i}$ is the contact torque, arising from the tangential and normal contact forces; \mathbf{R}_i is the rotation matrix from the global to the local coordinate system in which the calculation of the rotation expressed by Eq. (2) is accomplished.

As introduced by Favier et al. [35], the non-spherical particles are described by the overlapping multi-sphere model, as shown in Fig. 1(b). Thus, the interactions between any two non-spherical particles can be simplified as that of spherical particles. In this work, the elastic contact force is described by Hertz-Mindlin contact model [33], and the adhesive interaction is accounted for by JKR theory [36]:

$$F_n = \frac{4E^* a^3}{3R^*} - \sqrt{8\pi\Gamma E^*} a^{3/2} \quad (3)$$

where Γ is the interfacial surface energy; E^* is the equivalent Young's modulus; R^* is the equivalent radius; a is the contact radius. Based on Ferrari's solution [37], the contact radius a could be analytically calculated from the normal overlap α through this equation:

$$\alpha = \frac{a^2}{R^*} - \sqrt{\frac{2\pi\Gamma a}{E^*}} \quad (4)$$

The characteristic curve of the variation of F_n with α is shown in Fig. 2. In the unloading process, the normal contact force F_n is not zero when the normal overlap α is negative, as further work is required to separate the cohesive contact. More features and further information of the contact model are given by Thornton [33] and Pasha et al. [38], which are not shown here for brevity.

2.2. Simulation conditions

The simulation system comprises a spreading roller with diameter of 2 mm, and a rectangular base with length of $400D$, as shown in Fig. 3, where D represents the characteristic size D_{90} of particles by number. The front and rear boundaries (i.e. in the Y direction, namely perpendicular to the XZ plane shown in Fig. 3) of the simulation domain are treated as periodic boundaries for particle flow. Both the roller and base have the same width as the simulation domain in the Y direction, i.e. $10D$, for which the effect of domain width on the particle flow is minimised. To mitigate the bulk sliding of the particles, the base and roller are made up of clumped cylinders with axes along the Y direction, where the adjacent cylinders overlap 50% of the cylinder diameter. The cylinder diameter is equal to D for the base and $2D$ for the roller, resulting in fully-rough walls with the surface roughness of around Ra 3.2 μm and Ra 6.4 μm , respectively, where Ra represents the arithmetic mean deviation of the assessed surface profile, as calculated based on profilometry.

The initial particle bed is prepared by using the poured packing method, where approximately 21,000 particles are generated. For each size class shown in Fig. 1, several types of particles are randomly selected for simulating their shapes, with a total of 24 types of particle shapes used in the simulation. To make the computational time practical, Young's modulus in the simulation is 100 times smaller than the one measured in the experiment, and the surface energy is

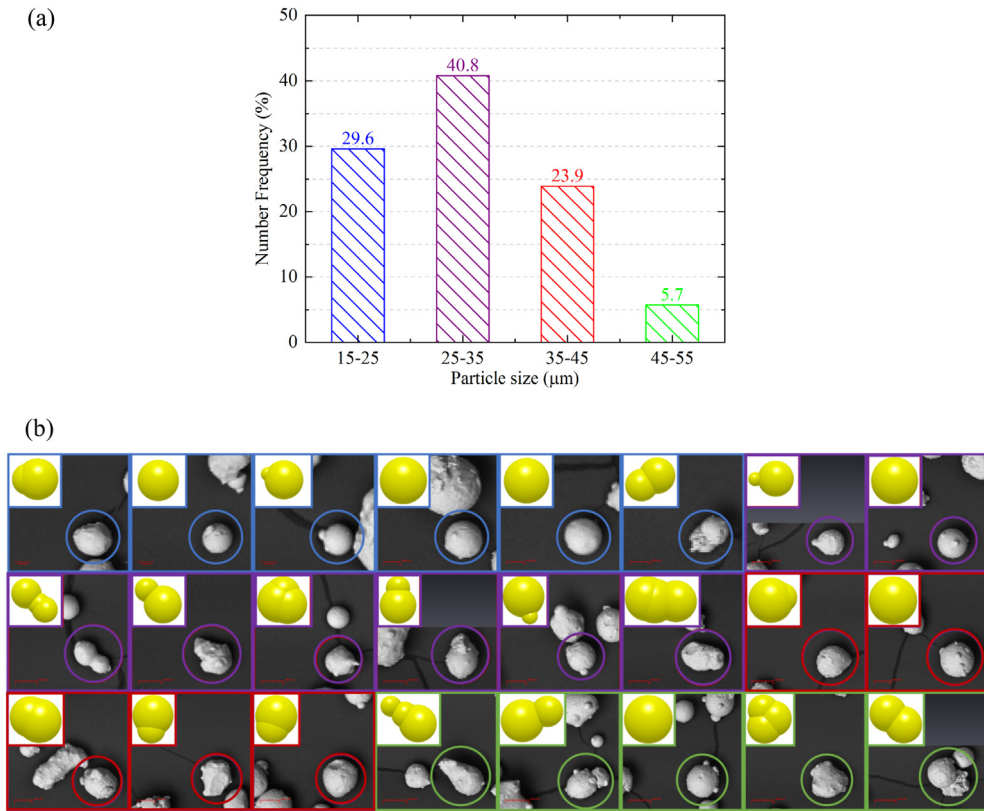


Fig. 1. Particle size distribution and particle shapes used in DEM simulations [20]. (a) Particle size distribution (equivalent-circle diameter) of gas atomised 316 L stainless steel particles classified into four size classes. (b) Particle shapes used in DEM simulations, together with the corresponding clumped spheres model; the shapes chosen for each size class are housed in colour boxes; six blue boxes (15–25 μm), eight purple boxes (25–35 μm), five red boxes (35–45 μm), and five green boxes (45–55 μm).

correspondingly scaled down in the simulation by keeping the Cohesive number of particle constant [39–41], as shown in Eq. (5). The physical and mechanical properties of particles, as used in the numerical simulation are given in Table 1. The roller and base are taken to be the same material as the particles, and the interaction parameters for particle-wall are the same as for particle-particle.

As the particle bed is generated, the roller spreader is placed at a specified position, forming a vertical gap of δ between the roller and base. As the particle spreading process begins, the roller moves along the X direction with a constant translational speed of U and rotates

anti-clockwise with a constant angular speed of ω , by which the particles are spread onto the rough base. The translational speed of roller is kept at $U = 0.08 \text{ m/s}$ in all cases. To evaluate the effect of spreading conditions on the particle flow and spread layer uniformity in the spreading process, the gap height δ/D is varied from 1.5 to 3.0, and the rotation speed ω is varied from 0 rad/s to 200 rad/s. When varying one parameter, the other one is kept constant if not specified, i.e. $\delta/D = 2.0$ or $\omega = 120 \text{ rad/s}$.

$$\text{Coh} = \frac{1}{\rho g} \left(\frac{\Gamma^5}{E^2 R^8} \right)^{1/3} \quad (5)$$

3. Simulation results

3.1. Effect of roller rotational speed

As the roller starts to rotate and move forward, a stable heap adjacent to the roller is generated and pushed forward. To explore the effect of roller rotational speed on the particle flow, two cases with and without roller rotation are compared. The velocity distribution of particles within the heap and the induced trajectories of representative particles are analysed.

As the roller operates, i.e. moves and rotates, several zones are formed within the heap due to the non-slip effects of the rough base and roller. To illustrate this, the particles in the heap are coloured into five classes (i.e. A-E) based on their velocity magnitude, as shown in Fig. 4, where the corresponding schematics are attached. The particle velocity has the smallest magnitude in block A, while the largest in block E. As shown in Fig. 4(a), the heap in the case of no roller rotation could be classified into three main zones: 1) zone I, the velocity blocks A,

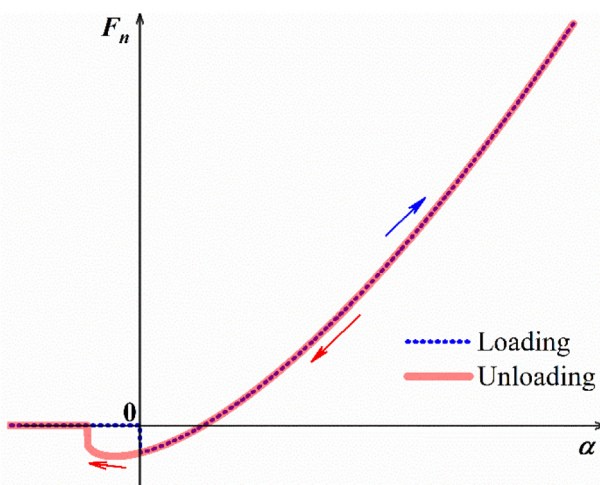


Fig. 2. The characteristic curve of the variation of the normal contact force with normal contact overlap.

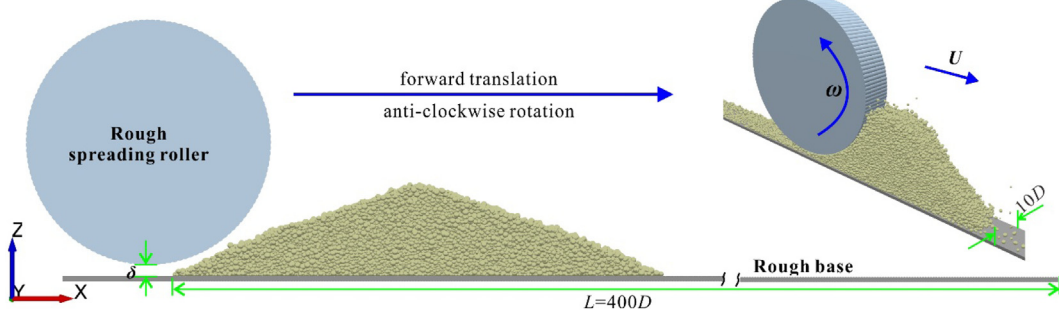


Fig. 3. Schematic diagram of simulation set-up for roller spreading process.

B and C, which are at the bottom of the heap; 2) zone II, the velocity block D, which is right above zone I; 3) zone III, the velocity block E, which is on the free surface and slope of the heap. In zone I, the velocity blocks (i.e. A, B and C) do not have distinct boundaries between each other. Due to particle acceleration under gravity, the particles in zone III (i.e. E) have the largest velocity. Compared to the zones I and III, zone II (i.e. D) occupies about 80% of the whole heap, and the topmost point of the heap is attached to the roller surface.

As shown in Fig. 4(b), the heap in the case with roller rotation could be also classified into three main zones: 1) zone I, the velocity blocks A, B and C; 2) zone II, part velocity block D and whole velocity block E, which are on the left side of the heap, with E being adjacent to the roller surface; 3) zone III, the velocity block D which is on the free surface at the top of the heap. In zone I, three velocity blocks (i.e. A, B and C) are all in cascading style, in analogy with cascading flow in drums, where the boundaries between them are in parabolic form. It is the most prominent feature of the heap, compared to the case without rotation ($\omega = 0 \text{ rad/s}$). Meanwhile, due to the action of roller rotation, the particles are cast far away and the topmost part of the heap does not touch the roller surface. The particles in zone II (i.e. E and part D) are strongly affected by the rotational speed of the roller. This zone is very narrow, i.e. a few particle diameters. Compared to zones II and III, zone I (i.e. A, B and C) occupies most of the whole heap.

To further illustrate the effect of roller rotational speed on the particle flow in the heap, the spatial positions of particles are recorded as a function of time and their motion is backtracked to illustrate the origin

of particles in the spread layer. For this purpose, the particles in two regions are backtracked: 1) the region with length of $4D$ (i.e. X direction) at the end of spread layer, i.e. at $t = 0.15 \text{ s}$, as shown in Fig. 5(a); 2) five regions with size $2D$ in both X and Z directions, which are initially around the roller at $t = 0.04 \text{ s}$, as shown in Fig. 5(b). For particles in the first region ($t = 0.15 \text{ s}$), they are backtracked to the beginning of the spreading process ($t = 0.0 \text{ s}$). To minimise the effects of the initial roller motion on the particle movement, the particles in the five regions, as shown in Fig. 5(b), are tracked from $t = 0.04 \text{ s}$ (i.e. the current position shown in Fig. 5(b)) to $t = 0.15 \text{ s}$ (i.e. the end of particle spreading process). The depth in Y direction is the same as the base, i.e. $10D$.

The trajectories of the particles, which end up in the box as shown in Fig. 5(a), are shown in Fig. 6, where the tracked particles are in red colour and other particles are transparent for better comparison. For the case without roller rotation, the trajectories of the tracked particles are classified into groups: 1) as the particle bed is pushed by the roller, the tracked particles are moved to higher positions, as shown in Fig. 6 (a1)-(c1); 2) they then avalanche down the slope of the heap, as shown in Fig. 6 (c1)-(i1); 3) they are then covered by the particles above them, and are slowed down by the non-slip effects of the rough base, and finally form the final spread layer, as shown in Fig. 6(i1)-(l1). For the case with roller rotation, a completely different pattern of motion prevails. The trajectories of the tracked particles show several distinct differences: 1) the particles that form the final tracked spread layer are more disperse in the initial heap, as shown in Fig. 6 (a2); 2) the ones on the lower positions are first collected at the left side of the heap, as shown in Fig. 6 (a2)-(c2); 3) the collected particles are then lifted up along the left side and then cascade down on the slope on the right side of the heap, as shown in Fig. 6 (g2)-(i2). Clearly, the trajectories of the tracked particles in the case with roller rotation are much longer than those without roller rotation. Interestingly, the particles in the box shown in Fig. 5 (a) are composed of particles from entirely different positions of the heap, i.e. the red particles in Fig. 6 (a2) give rise to this tiny region shown in Fig. 6 (l2).

The trajectories of particles around the roller (i.e. Fig. 5(b)) are shown in Fig. 7, where the tracked particles in five cells are in red, blue, green, black and orange colours, respectively, while other particles are transparent for better comparison. The initial positions (i.e. 0.04 s) of the tracked particles are shown in Fig. 5(b). The first time sequences a1

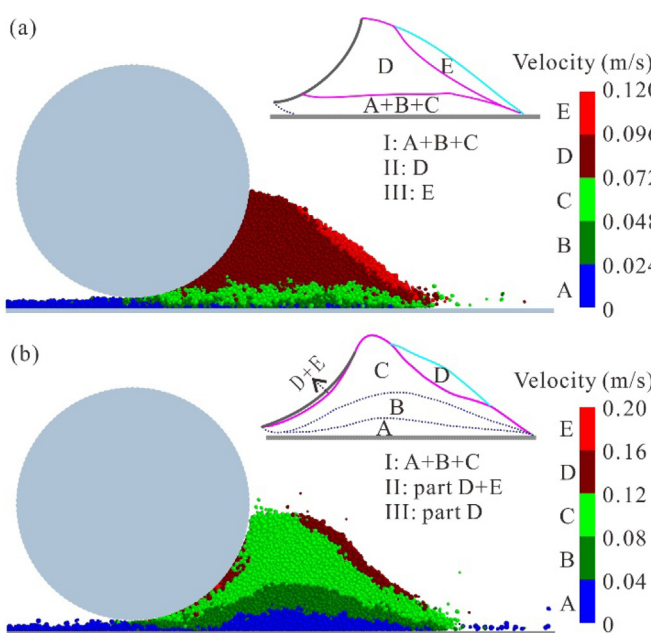


Fig. 4. Velocity distribution of particles in the heap which is classified into zones I-III, for cases with (a) $\omega = 0 \text{ rad/s}$ and (b) $\omega = 120 \text{ rad/s}$.

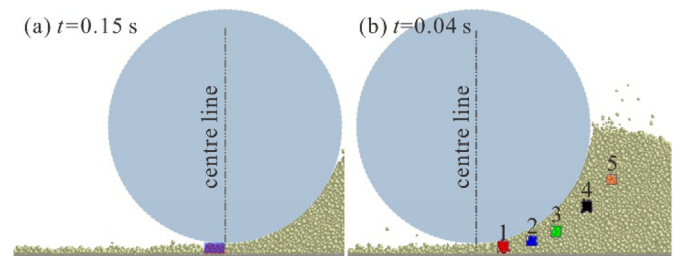


Fig. 5. The illustration of the selected particles for backtracking in two regions (a) at the end of spread layer at $t = 0.15 \text{ s}$ and (b) around the roller at $t = 0.04 \text{ s}$.

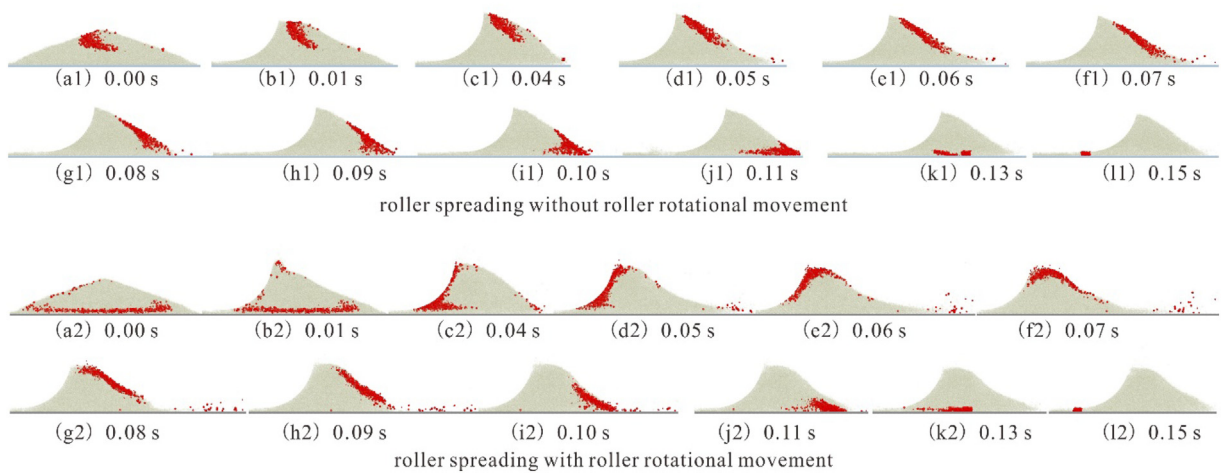


Fig. 6. Temporal sequence of the spatial positions of the particles in the region shown in Fig. 5(a).

and a2 here relate to 0.05 s after the start of simulation. For the case without roller rotation, the particles in cells 1 and 2 (i.e. red and blue colours) are spread onto rough base in a short time, while all the particles in cell 4 (i.e. black colour) move along with the roller. The particles in cell 3 (i.e. green colour) are spread very slowly, and most of them remain on the left side of the heap with almost constant relative positions. As the particles are spread onto the rough base, the heap becomes smaller with time. Under this effect, the particles in cell 5 (i.e. orange colour) reach the free surface of the heap and then cascade down

along the slope under gravity. Thus, the particles in this case move directly to the rough base by first reaching the right edge of the heap.

For the case with roller rotation, the trajectories of the tracked particles show several distinct differences from the no-rotation case: 1) apart from some particles in cell 1 spreading onto the rough base quickly, the rest (i.e. red colour) and all the particles in cell 2 (i.e. blue colour) and some of cell 3 (i.e. green colour) are lifted up by the roller and then cascade down on the heap slope before spreading onto the rough base; 2) the rest of the particles in cell 3 circulate along the edges of the

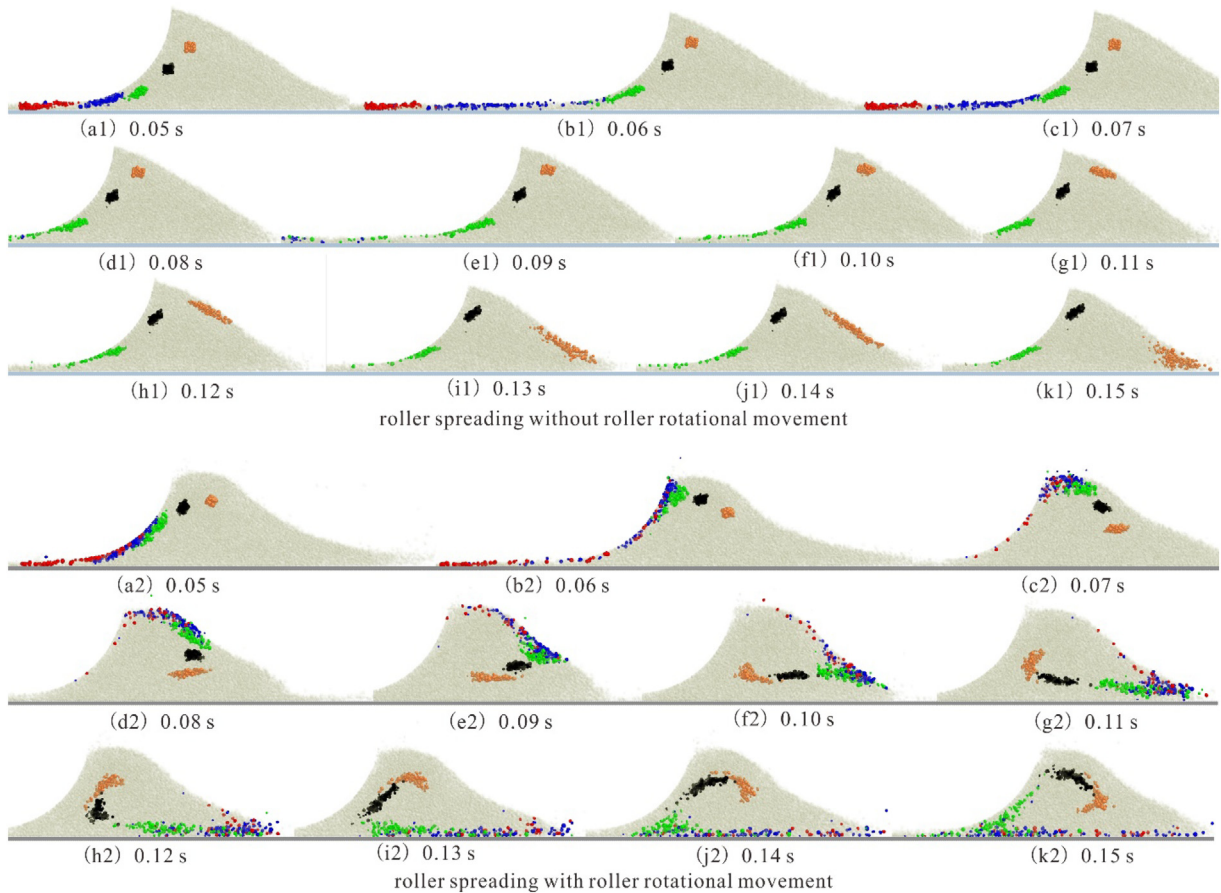


Fig. 7. Temporal sequence of the spatial positions of the particles in five cells around the roller shown in Fig. 5(b), cell 1-red colour, cell 2-blue colour, cell 3-green colour, cell 4-black colour, cell 5-orange colour.

heap (i.e. the left and right sides and the bottom); 3) all the particles in cells 4 and 5 (i.e. green colour and black colour) are first lifted up by the roller, and then are dragged in by the bulk circulation within the heap; 4) some of the particles in cell 3 are slowed down when moving along the rough base and are then collected and lifted up again by the roller. Thus extensive convection and circulation of particles take place within the heap during the spreading process.

To better illustrate the particle dynamics in the heap, the averaged trajectories of the particles in these five cells are also recorded, as shown in Fig. 8, where the abscissa is the relative position of the particle centre x with respect to the roller centre x_c . For the case without roller rotation, the particles move in very simple ways with a short route, such as straight towards the rough base or down along the slope of the heap, in agreement with Fig. 7. For the case of roller rotation, the particles have much longer routes with more diversity. Fig. 8(b) is consistent with particle trajectories shown in Fig. 7: spreading onto the base for cell 1, lifting and cascading movement for cell 2, edge-circulation for cell 3, and inner-circulation for cells 4 and 5. This gives rise to extensive convection and circulation of the particles.

3.2. Particle spread layer

When particle spreading is finished, a thin layer of particles is formed on the rough base. Good particle spreading means a dense

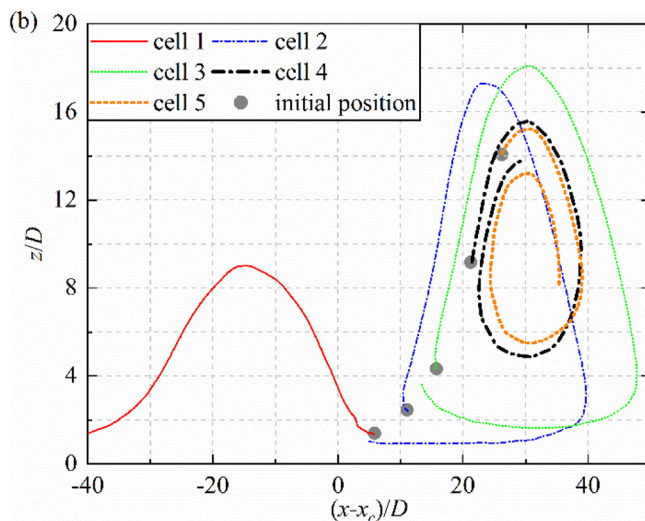
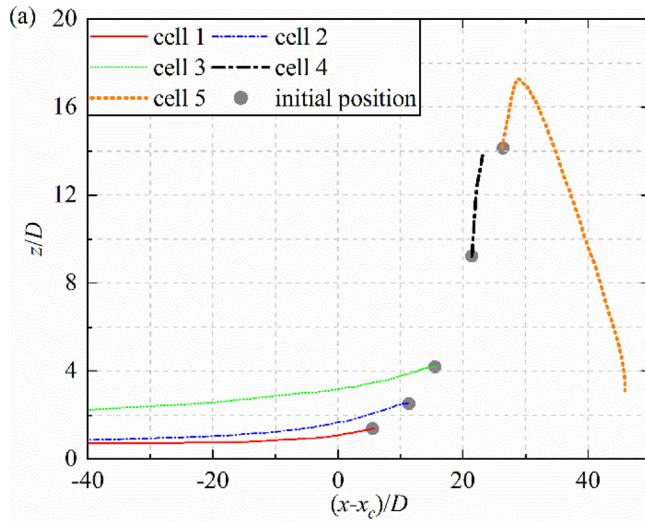


Fig. 8. Averaged trajectories of the particles in five tracking cells for (a) $\omega = 0$ rad/s and (b) $\omega = 120$ rad/s.

uniform spread layer, i.e. unvarying particle size distribution (PSD) along the spreading direction and no empty patches. If the PSD of the spread layer is different from that of the initial bulk particle bed, the segregation of particles is implied in the spreading process. Considering that a small gap is required for spreading a thin layer, it is likely that segregation could readily occur if the PSD is wide. Therefore the packing and segregation extent of particles in the spread larger are analysed.

The total volume of particles V_{layer} of the spread layer is normalised as:

$$V_{layer} = \frac{\sum V_p}{LWD} \quad (6)$$

where V_p is the volume of an individual particle; L is the length of the spread layer (i.e. in the X direction); W is the width of the spread layer (i.e. in the Y direction). The effects of the gap height and roller rotational speed on total particle volume are shown in Fig. 9(a), where an almost linear trend is observed for the former. The effect of the latter has been analysed for one gap height only, and the results are shown in the inset. For a monolayer coverage Fig. 9(a) actually represents the fractional area covered by the particles. Alternatively, the volume of the spread particles can be normalised with respect to the swept volume by the roller by re-expressing Eq. (6) in terms of the effective gap height, i.e. $(\delta - \delta_c)$, where δ_c is the critical gap height at which the mass flow rate is zero, accounting for dynamic boundary effects of the spreader. The results are shown in Fig. 9(b), where the data points have small fluctuations around 0.56, indicating that particles flow varies linearly with the effective gap height within the range analysed. It is noteworthy that $\delta_c = 1.25D$ in this case, in contrast to that of the blade spreader for which $\delta_c = D$ for the same particle system as reported by Nan et al. [21]. This implies that the counter-rotation of the roller has a retarding effect on the flow of particles underneath the roller, as intuitively expected. Following the approach of Nan et al. [21] for the blade spreading process, the mass flow rate of particles, M , through the gap is given as:

$$M = \rho f_u W(\delta - \delta_c) \quad (7)$$

where ρ is the particle density; f_u is a function of the translational velocity of the spreader. So $\sum V_p$ can be estimated from Mt/ρ and the normalised spread particle volume, V_{layer} , is given as:

$$V_{layer} = \frac{Qt}{\rho LWD} = k_{layer} \frac{\delta - \delta_c}{D} \quad (8)$$

$$k_{layer} = \frac{f_u Ut}{U L} = \frac{f_u}{U} \quad (9)$$

where L is the length of particle spread layer, given by $L = Ut$, where t is the spreading time and U is the spreader translational speed. By using the least square fitting method, $k_{layer} = 0.56$ and $\delta_c/D = 1.25$ are obtained in this work. These equations have previously been applied to the blade spreading, for which $k_{layer} = 0.55$ with a deviation of $\pm 10\%$, when the blade spreading speed is below a threshold for which a linear trend prevails [21]. As the roller spreading process involves both translational and rotational movements of the spreader, k_{layer} is a complex function of U and ω . Its characterisation requires further extensive work for developing a regime map as a function of spreading variables.

With the increase of roller rotational speed, the convection/circulation of particle flow in the heap increases, as the particles are more easily entrained by the roller movement. Thus, fewer particles are spread onto the base, resulting in a large decrease of the total particle volume as shown in the inset of Fig. 9(a). The rate of decrease is fast for 40 rad/s and 120 rad/s rotational speeds. The total particle volume in the case of no roller rotation (i.e. $\omega = 0$ rad/s) is much larger than that with roller rotation. This suggests that the parameter k_{layer} in

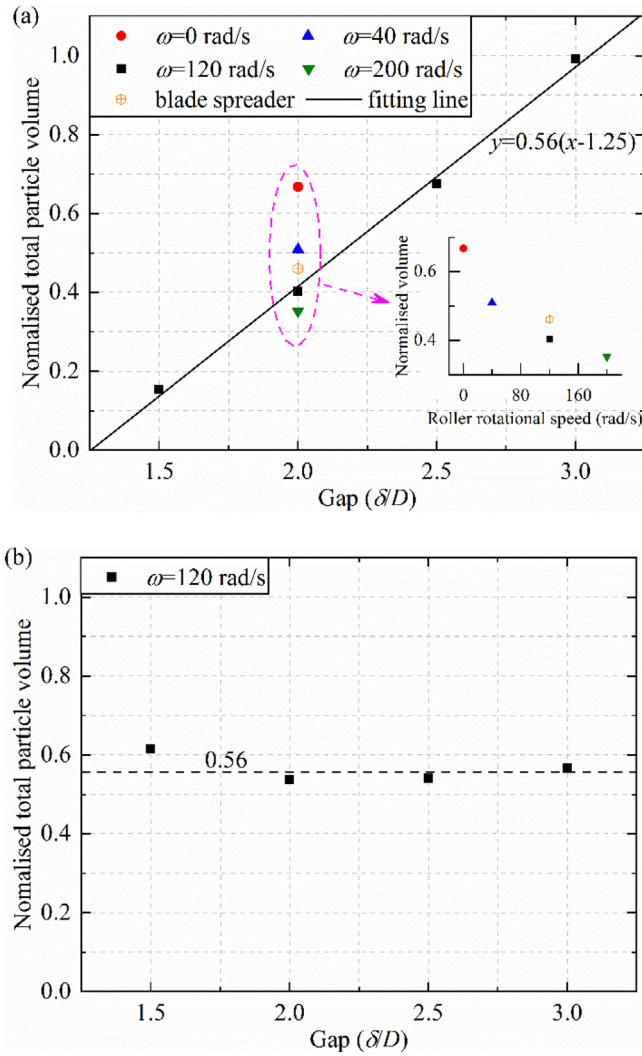


Fig. 9. Variation of the total particle volume of spread layer with the gap height and roller rotational speed: (a) normalised by particle diameter D ; (b) normalised by effective gap height, i.e. $(\delta - \delta_c)$.

Eq. (8) is strongly affected by roller rotational movement, even when the roller rotational speed is small.

The spread layer of roller spreading is also compared to that of blade spreading in Fig. 9(a), where the same translation speed (i.e. 0.08 m/s)

as the roller is used. Haeri et al. [17] stated that the roller spreading outperforms the blade spreading under the same translation velocity of spreader in terms of total particle volume of spread layer, due to larger contact area allowing for gradual particle rearrangement. However, as shown in Fig. 9(a), the roller spreading could get denser spread layer only when the roller rotational speed is small. This implies that there should be a transitional roller rotational speed, below which the roller outperforms the blade spreader at the same translational spreading speed. However, the translational and rotational speeds have a coupled effect. Moreover, the fluid medium (commonly air or nitrogen) would exert an influence on the particle flow in the heap, particularly for fine particles which could get partially or even fully fluidised, due to the roller action. So it is likely that these dynamics could affect the transient jamming, aspects which require further research.

Images of the final spread layer deposited by the roller are shown in Fig. 10, where the particles are spread from left to right and are coloured based on their volume. For the small gap height (i.e. $\delta/D = 1.5$), a number of empty patches are evident along the spreading direction. The pattern is similar to that obtained by blade spreading, for which the frequency and length of empty patches have been analysed by Nan et al. [20]. It appears that for a given gap height, the uniformity of spreading deteriorates as the roller rotational speed is increased, as more empty patches are observed. Along with the formation of empty patches, the segregation of particles is also observed in the spread layer. For example, in the case of $\delta/D = 1.5$, the last 1/3 length of the spread layer is almost devoid of large particles, shown by red colour. With the increase of the gap height or decrease of roller rotational speed, fewer empty patches are found, and the spread layer becomes denser with more uniform distribution of particles.

To further depict particle size distribution in the spread layer, the particles are sorted into the same four classes as in Fig. 1, i.e. 15–25 μm , 25–35 μm , 35–45 μm and 45–55 μm . In order to reduce the effect of the roller initial motion, the last 6 mm length of the spread layer is analysed. The number frequency of the four particle size classes is shown in Fig. 11, together with that of the initial particle bed before spreading for comparison. For the case of $\delta/D = 1.5$, the number frequency of the size class 25–35 μm remains the same as the PSD of the initial particle bed, whilst for the other three size classes there are notable deviations. For example, the number frequency for 15–25 μm and 45–55 μm particles is about 160% and 16% of the initial particle bed, respectively. This trend suggests that more small particles and fewer large particles are spread on the base for this narrow gap, which is in accordance with the images of the spread layer shown in Fig. 10(a). When the gap height (δ/D) is increased to 2.0, the deviation of the number frequency of particles from that of the initial particle bed decreases significantly, especially for the smallest and 35–45 μm size classes. However,

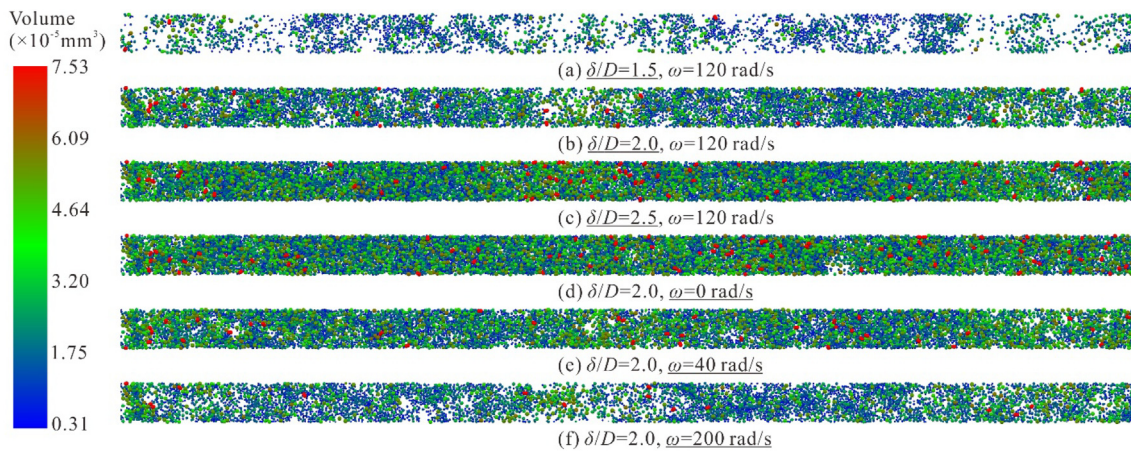


Fig. 10. Images of the spread layers for three gap heights and four roller rotational speeds, with the roller translational velocity at 0.08 m/s.

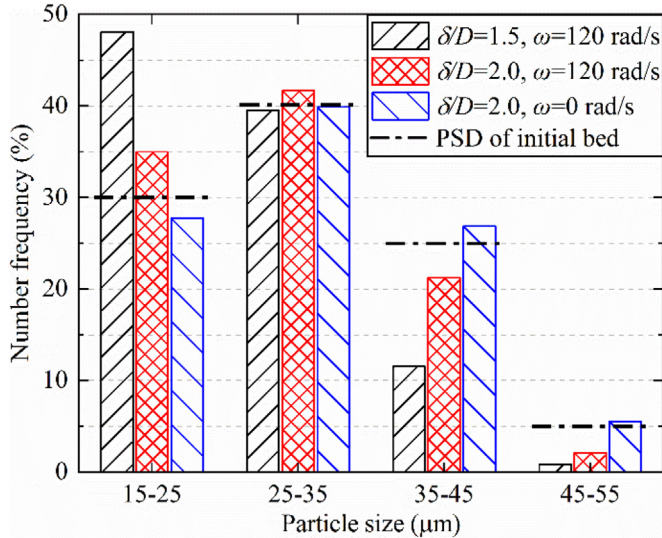


Fig. 11. The number frequency of particles of the spread layer and initial particle bed.

the deviation is still large for 45–55 μm particles. For $\omega = 120$ rad/s, the number frequency is about 40% of the initial value. This indicates that the extent of segregation depends strongly on the size classes of particles. When the roller rotational speed decreases from 120 rad/s to 0 rad/s, the number frequency is very close to that of the initial particle bed, resulting in a better performance. The deviation for all particle size classes is less than 10%, suggesting that the rotational movement of the roller promotes particle segregation.

In order to assess the local variation of the segregation extent along the spreading direction (i.e. the X direction), the spread layer is divided into five identical cells, with the same width as the base in the Y direction and the maximum height of spread layer in the Z direction. For each size class of particles (i.e. $j = 1-4$, which stands for 15–25 μm, 25–35 μm, 35–45 μm and 45–55 μm, respectively), its number percentage x_{ji} in each cell (i.e. $i = 1-5$) is calculated, and the segregation index SI_j is calculated:

$$SI_j = \frac{\sigma_j}{x_{j0}} \quad (10)$$

where x_{j0} is the number percentage of particle size class j in the initial particle bed before spreading; σ_j is the deviation of x_{ji} from x_{j0} in all cells, given as:

$$\sigma_j^2 = \sum_{i=1}^N \frac{w_i(x_{ji}-x_{j0})^2}{\sum_{i=1}^N w_i} \quad (11)$$

where w_i is the total number of all particles in cell i , and $N = 5$ is the number of cells. The segregation index SI_j equals to zero if the number percentage of particle j in every cell is identical to that of the initial particle bed.

The effect of gap height on the segregation index is shown in Fig. 12 (a) for the roller rotational speed of 120 rad/s. For the gap height of $\delta/D = 1.5$, the segregation index is the largest for all size classes of particles, especially for 45–55 μm particles. As the gap height (δ/D) increases to 2.0, the segregation index decreases sharply. For example, the segregation index drops from 0.73 to 0.31 for 15–25 μm particles. With further increase of the gap height, the segregation index for the largest particle size class (i.e. 45–55 μm) continues to decrease, but it changes only slightly for other size classes. This suggests that uniform spreading of large particles in the tail end of PSD requires larger gap heights than that for small particles.

The effect of the roller rotational speed on the segregation index is shown in Fig. 12(b) for the gap height $\delta/D = 2.0$. For the case of no roller

rotation, the segregation index is the smallest. As the roller rotational speed is increased, the segregation index increases sharply, especially for the largest particles. According to Fig. 12(a)–(b), the segregation index of 45–55 μm particles is the largest in all cases, indicating that large particles undergo segregation to a larger extent during the spreading process. The segregation index of large particles is more sensitive to the gap height and roller rotational speed than that of small particles.

3.3. Segregation mechanisms in powder spreading process

The segregation mechanisms due to particle shearing flow have been widely investigated, which could be categorised as percolation/sifting segregation [42–44], trajectory segregation [45], fluidisation and elutriation segregation [46–48], and agglomeration segregation [49–51]. However, these mechanisms are mainly based on bulk flow through hoppers, moving beds, chutes, and heap formation, etc. In the particle spreading process, the gap is narrow for making a thin particle layer. The quality of spread layer and extent of segregation are therefore more affected by the near-boundary flow between the walls of spreader and base. Thus, particle segregation in the spreading process is different to those in traditional bulk particle flows, especially for its strong dependence on the gap height.

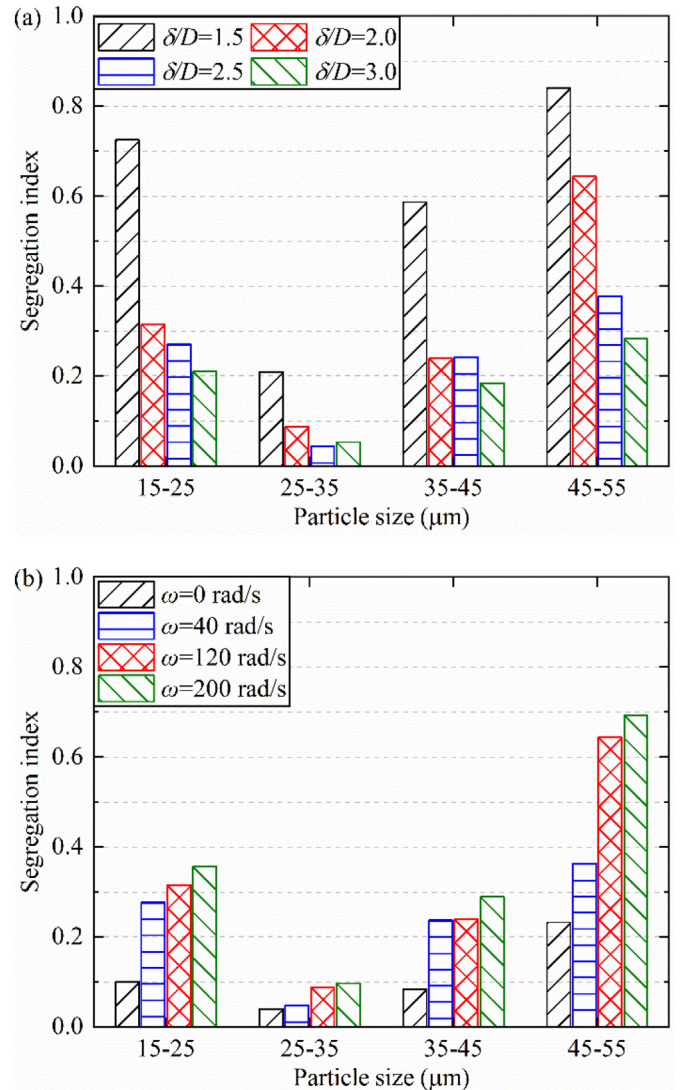


Fig. 12. Variation of the segregation index of spread layer with (a) gap height at $\omega = 120$ rad/s and (b) roller rotational speed at $\delta/D = 2.0$.

As the gap height and roller rotational speed affect both the total particle volume and segregation extent of the spread layer, the variation of the mean segregation index SI with the total particle volume V_{layer} is analysed and shown in Fig. 13, where SI is the average segregation index of the four size classes of particles SI_j . It shows that the mean segregation index decreases with the total particle volume of the spread layer when varying solely either the gap height or roller rotational speed. This suggests that the more particles flow through the gap, the fewer large particles are trapped in the heap, implying of course large gaps or small roller rotational speed. However, the mechanisms of these two situations are different, as detailed in the following. It is noteworthy that for the same total particle spread volume, in order to reduce the segregation extent, it is more effective to decrease the roller rotational speed than increasing the gap height.

The extensive segregation in the spread layer at the gap height of $\delta/D = 1.5$ is related to the occurrence of transient particle jamming in the narrow and confined region between the rough roller and base. This is revealed by the time-averaged roller force in the spreading direction (normalised with respect to the total weight of the particles in front of the roller, i.e. on the right side of the vertical centre line of the roller) as shown in Fig. 14. For the case of $\delta/D = 1.5$, the roller force is roughly 20 times larger than the total weight of particles, which is caused by the strong contact force network formed during the survival period of particle jamming. As particle jamming is sensitive to the relative size between the particles and gap height, the frequency and survival time of jamming events is different for large and small particles. At the specified gap height, large particles tend to have more jamming events with longer survival time, resulting in more particles halted in the heap for a longer time without spreading onto the rough base. Meanwhile, as the roller continues to move forward, the jamming state is broken with the collapse of arches, resulting in a sudden release of the elastic energy stored in the contact force network. Under this effect, the jammed particles and their neighbouring particles ‘fly’ through the gap in the opposite direction of the spreading. Due to smaller size and inertia moment, small particles tend to be pushed through the gap more freely following the collapse of arches. Under the combined effects of these two mechanisms, an extensive segregation of spread layer is caused by jamming when the particles flow through the narrow gap (i.e. $\delta/D = 1.5$). When the gap height (δ/D) is increased to 2.0 or larger, the normalised roller force is sharply reduced, which is due to the decrease of the frequency and survival time of particle jamming. Thus, the size segregation during the jamming period and the following arch collapse is reduced.

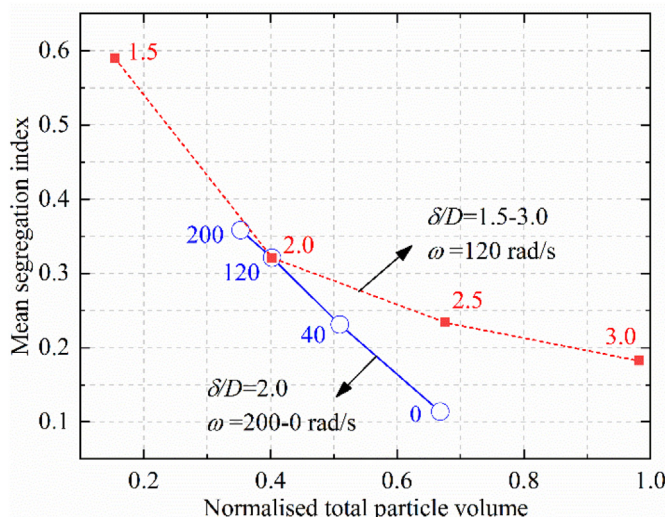


Fig. 13. Variation of mean segregation index and normalised total particle volume of spread layer with gap height and roller rotational speed.

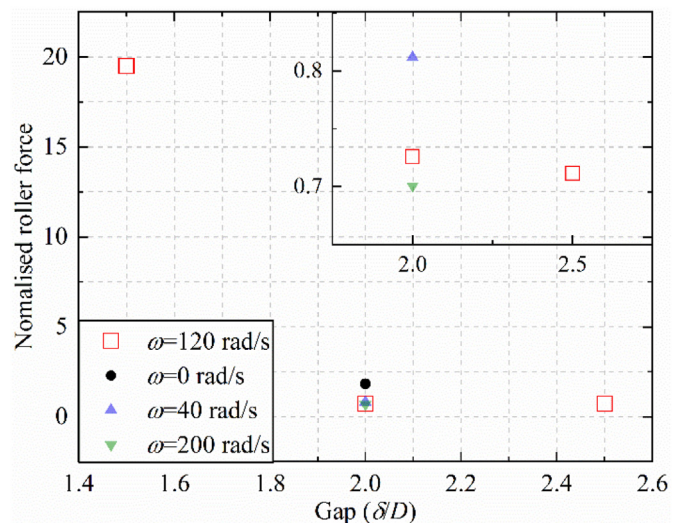


Fig. 14. Variation of the total roller force with gap height and roller rotational speed.

The lowest segregation index in the case of no roller rotation is related to the simple flow pattern in the heap without any particle convection and circulation, as shown in Fig. 7. The particles move almost as a plug, and the segregation is affected mainly by particle jamming. As the roller rotational movement is applied to the heap, extensive convection and circulation of particles take place in the heap as shown in Fig. 7. The particles move in much longer trajectory before spreading onto the base. Due to the differences in inter-particle interactions and in particle size, and the presence of shearing flows in the heap, the segregation could occur before the particles even reaching the gap. It is further enhanced by the jamming events as the particles flow through the gap. With the increase of roller rotational speed, the intensity of the convection/circulation increases, resulting in even more extensive segregation of particles, enhanced by the jamming events.

4. Conclusions

The particle spreading process with a roller spreader has been analysed by DEM simulations, using realistic physical and mechanical properties of particles as measured for single particles in the previous work. The effect of gap height and roller rotational speed on the spreading has been analysed and quantified in terms of the trajectories of particles in the heap and formation of empty patches and segregation of the spread layer. The main results from the present study are summarised as follows:

- 1) Notable convection and circulation of particles take place in the heap when the roller rotational movement is applied, due to the cascading style distribution of particle velocity. Before spreading onto the rough base, the particles are lifted up along the left side of the heap by the action of roller rotation, and then avalanche down along the right side of the heap due to gravity.
- 2) The variation of the total particle volume of spread layer with gap height is described by an empirical linear equation. At the same translational velocity, the roller outperforms the blade spreader in terms of total particle volume of spread layer only at small roller rotational speeds.
- 3) Extensive size segregation is observed in the spread layer for the narrow spreading gaps. With the increase of gap height or decrease of roller rotational speed, a spread layer with less particle segregation could be obtained. Compared to small particles, large particles undergo more extensive segregation and their segregation index is more sensitive to the gap height and the roller rotational speed.

- 4) The segregation of the spread layer is related to the jamming events of the near-boundary flow between the rough roller and base. Jamming is sensitive to the relative size between particles and gap height. The roller rotational movement enhances the particle segregation by turning over the heap. As compared to blade spreading, roller spreading causes more segregation, so in general it should be less suitable for free flowing particles with a wide size distribution. In contrast, fine cohesive particle systems are less prone to segregation even for relatively wide PSD. Particle shearing in the heap by the combined translational and rotational movement of the roller could break the cohesion-induced agglomerates, so roller spreading could in principle also produce a satisfactory spreading performance.

Declaration of Competing Interest

The authors declare that they have no known competing financial interests or personal relationships that could have appeared to influence the work reported in this paper.

Acknowledgements

The support of the Virtual Formulation Laboratory Grant of the EPSRC Future Formulation Programme (EP/N025261/1) is gratefully acknowledged. The first author is grateful to the National Natural Science Foundation of China (Grant No. 51806099) for the financial support of part of this work. The authors are also thankful to DEM Solutions, Edinburgh, UK, for providing a special license for the EDEM software for use in this work.

References

- [1] S. Antoniw, N. McCarthy, E. Pacey, B. Parkin, P. Shelton, Additive manufacturing: opportunities and constraints, Royal Acad. Eng. (2013) 1–21.
- [2] B. Berman, 3-D printing: the new industrial revolution, *Business Horizons* 55 (2012) 155–162.
- [3] U.M. Dilberoglu, B. Gharehpapagh, U. Yaman, M. Dolen, The role of additive manufacturing in the era of industry 4.0, *Procedia Manuf.* 11 (2017) 545–554.
- [4] T. DebRoy, H.L. Wei, J.S. Zuback, T. Mukherjee, J.W. Elmer, J.O. Milewski, A.M. Beese, A. Wilson-Heid, A. De, W. Zhang, Additive manufacturing of metallic components – process, structure and properties, *Prog. Mater. Sci.* 92 (2018) 112–224.
- [5] W.E. Frazier, Metal additive manufacturing: a review, *J. Mater. Eng. Perform.* 23 (2014) 1917–1928.
- [6] N. Shamsaei, A. Yadollahi, L. Bian, S.M. Thompson, An overview of direct laser deposition for additive manufacturing: part II: mechanical behavior, process parameter optimization and control, *Additive Manuf.* 8 (2015) 12–35.
- [7] T.D. Ngo, A. Kashani, G. Imbalzano, K.T.Q. Nguyen, D. Hui, Additive manufacturing (3D printing): a review of materials, methods, applications and challenges, *Compos. Part B* 143 (2018) 172–196.
- [8] S.M. Thompson, L. Bian, N. Shamsaei, A. Yadollahi, An overview of direct laser deposition for additive manufacturing; part I: transport phenomena, modeling and diagnostics, *Additive Manuf.* 8 (2015) 36–62.
- [9] I. Gibson, D. Rosen, B. Stucker, *Additive Manufacturing Technologies, 3D Printing, Rapid Prototyping, and Direct Digital Manufacturing*, Springer, 2015.
- [10] N. Guo, M.C. Leu, Additive manufacturing: technology, applications and research needs, *Front. Mech. Eng.* 8 (2013) 215–243.
- [11] D.D. Gu, W. Meiners, K. Wissenbach, R. Poprawe, Laser additive manufacturing of metallic components: materials, processes and mechanisms, *Int. Mater. Rev.* 57 (2013) 133–164.
- [12] S. Singh, S. Ramakrishna, R. Singh, Material issues in additive manufacturing: a review, *J. Manuf. Process.* 25 (2017) 185–200.
- [13] A. Townsend, N. Senin, L. Blunt, R.K. Leach, J.S. Taylor, Surface texture metrology for metal additive manufacturing: a review, *Precis. Eng.* 46 (2016) 34–47.
- [14] S.A. Khairallah, A.T. Anderson, A. Rubenchik, W.E. King, Laser powder-bed fusion additive manufacturing: physics of complex melt flow and formation mechanisms of pores, spatter, and denudation zones, *Acta Mater.* 108 (2016) 36–45.
- [15] P. Bidare, R.R.J. Maier, R.J. Beck, J.D. Shephard, A.J. Moore, An open-architecture metal powder bed fusion system for in-situ process measurements, *Additive Manuf.* 16 (2017) 177–185.
- [16] E.J.R. Parteli, T. Pöschel, Particle-based simulation of powder application in additive manufacturing, *Powder Technol.* 288 (2016) 96–102.
- [17] S. Haeri, Y. Wang, O. Ghita, J. Sun, Discrete element simulation and experimental study of powder spreading process in additive manufacturing, *Powder Technol.* 306 (2016) 45–54.
- [18] H. Chen, Q. Wei, S. Wen, Z. Li, Y. Shi, Flow behavior of powder particles in layering process of selective laser melting: numerical modeling and experimental verification based on discrete element method, *Int. J. Mach. Tools Manuf.* 123 (2017) 146–159.
- [19] S. Haeri, Optimisation of blade type spreaders for powder bed preparation in additive manufacturing using DEM simulations, *Powder Technol.* 321 (2017) 94–104.
- [20] W. Nan, M. Pasha, T. Bonakdar, A. Lopez, U. Zafar, S. Nadimi, M. Ghadiri, Jamming during particle spreading in additive manufacturing, *Powder Technol.* 338 (2018) 253–262.
- [21] W. Nan, M. Ghadiri, Numerical simulation of powder flow during spreading in additive manufacturing, *Powder Technol.* 342 (2019) 801–807.
- [22] C. Meier, R. Weissbach, J. Weinberg, W.A. Wall, A.J. Hart, Critical influences of particle size and adhesion on the powder layer uniformity in metal additive manufacturing, *J. Mater. Process. Technol.* 266 (2019) 484–501.
- [23] C. Meier, R. Weissbach, J. Weinberg, W.A. Wall, A. John Hart, Modeling and characterization of cohesion in fine metal powders with a focus on additive manufacturing process simulations, *Powder Technol.* 343 (2019) 855–866.
- [24] Q. Han, H. Gu, R. Setchi, Discrete element simulation of powder layer thickness in laser additive manufacturing, *Powder Technol.* 352 (2019) 91–102.
- [25] E. Herbold, O. Walton, M. Homel, Simulation of Powder Layer Deposition in Additive Manufacturing Processes Using the Discrete Element Method, Lawrence Livermore National lab.(LLNL), Livermore, CA (United States, 2015).
- [26] H.W. Mindt, M. Megahed, N.P. Lavery, M.A. Holmes, S.G.R. Brown, Powder bed layer characteristics: the overseen first-order process input, *Metall. Mater. Trans. A* 47 (2016) 3811–3822.
- [27] W. Zhang, A. Mehta, P.S. Desai, C.F. Higgs, Machine learning enabled powder spreading process map for metal additive manufacturing (AM), *Int. Solid Free Form Fabr. Symp.* Austin, TX 2017, pp. 1235–1249.
- [28] Y.S. Lee, P. Nandwana, W. Zhang, Dynamic simulation of powder packing structure for powder bed additive manufacturing, *Int. J. Adv. Manuf. Technol.* 96 (2018) 1507–1520.
- [29] Y.M. Fouda, A.E. Bayly, A DEM study of powder spreading in additive layer manufacturing, *Granul. Matter* 22 (2019).
- [30] H. Chen, Q. Wei, Y. Zhang, F. Chen, Y. Shi, W. Yan, Powder-spreading mechanisms in powder-bed-based additive manufacturing: experiments and computational modeling, *Acta Mater.* 179 (2019) 158–171.
- [31] P.S. Desai, C.F. Higgs, Spreading process maps for powder-bed additive manufacturing derived from physics model-based machine learning, *Metals* 9 (2019) 1176.
- [32] P.A. Cundall, O.D.L. Strack, A discrete numerical model for granular assemblies, *Géotechnique* 29 (1979) 47–65.
- [33] C. Thornton, *Granular Dynamics, Contact Mechanics and Particle System Simulations*, Springer, New York, 2015.
- [34] W. Nan, M. Ghadiri, Y. Wang, Analysis of powder rheometry of FT4: effect of particle shape, *Chem. Eng. Sci.* 173 (2017) 374–383.
- [35] J.F. Favier, M.H. Abbaspour-Fard, M. Kremmer, A.O. Raji, Shape representation of axisymmetrical, non-spherical particles in discrete element simulation using multi-element model particles, *Eng. Comput.* 16 (1999) 467–480.
- [36] K. Johnson, K. Kendall, A. Roberts, Surface energy and the contact of elastic solids, *Proc. R. Soc. Lond. A Math. Phys. Sci.* 324 (1971) 301–313.
- [37] G.A. Korn, T.M. Korn, *Mathematical Handbook for Scientists and Engineers: Definitions, Theorems, and Formulas for Reference and Review*, Courier Corporation, New York, 2000.
- [38] M. Pasha, S. Dogbe, C. Hare, A. Hassanpour, M. Ghadiri, A linear model of elasto-plastic and adhesive contact deformation, *Granul. Matter* 16 (2014) 151–162.
- [39] M.A. Behjani, N. Rahmanian, N. Fardina bt Abdul Ghani, A. Hassanpour, An investigation on process of seeded granulation in a continuous drum granulator using DEM, *Adv. Powder Technol.* 28 (2017) 2456–2464.
- [40] J. Hærvig, U. Kleinhans, C. Wieland, H. Spliethoff, A.L. Jensen, K. Sørensen, T.J. Condra, On the adhesive JKR contact and rolling models for reduced particle stiffness discrete element simulations, *Powder Technol.* 319 (2017) 472–482.
- [41] K. Washino, E.L. Chan, T. Tanaka, DEM with attraction forces using reduced particle stiffness, *Powder Technol.* 325 (2018) 202–208.
- [42] P. Tang, V.M. Puri, An innovative device for quantification of percolation and sieving segregation patterns-single component and multiple size fractions, *Part. Sci. Technol.* 23 (2005) 335–350.
- [43] A.K. Jha, V.M. Puri, Percolation segregation of multi-size and multi-component particulate materials, *Powder Technol.* 197 (2010) 274–282.
- [44] P. Tang, V.M. Puri, Percolation segregation model for similar and differing constituents, *Part. Sci. Technol.* 28 (2010) 287–297.
- [45] W.R. Ketterhagen, J.S. Curtis, C.R. Wassgren, A. Kong, P.J. Narayan, B.C. Hancock, Granular segregation in discharging cylindrical hoppers: a discrete element and experimental study, *Chem. Eng. Sci.* 62 (2007) 6423–6439.
- [46] Y. Guo, C.Y. Wu, K.D. Kafui, C. Thornton, 3D DEM/CFD analysis of size-induced segregation during die filling, *Powder Technol.* 206 (2011) 177–188.

- [47] Y. Guo, C.Y. Wu, C. Thornton, The effects of air and particle density difference on segregation of powder mixtures during die filling, *Chem. Eng. Sci.* 66 (2011) 661–673.
- [48] F.P. Di Maio, A. Di Renzo, V. Vivacqua, A particle segregation model for gas-fluidization of binary mixtures, *Powder Technol.* 226 (2012) 180–188.
- [49] P. Tang, V.M. Puri, Methods for minimizing segregation: a review, *Part. Sci. Technol.* 22 (2004) 321–337.
- [50] M. Poux, P. Fayolle, J. Bertrand, D. Bridoux, J. Bousquet, Powder mixing - some practical rules applied to agitated systems, *Powder Technol.* 68 (1991) 213–234.
- [51] R. Hogg, Mixing and segregation in powders: evaluation, mechanisms and processes, *KONA Powder Particle J.* 27 (2009) 3–17.